

Communication

A Dual-Band Carbon Dioxide Sensor Based on Metal–TiO₂–Metal Metasurface Covered by Functional Material

Wei Long ^{1,2,†}, Rujun Zhou ^{1,2,†}, Zixuan Du ^{1,2}, Qiang Ling ¹ , Yusheng Zhang ¹, Ding Zhao ³ , Jie Shao ², Si Luo ^{1,*} and Daru Chen ¹¹ Hangzhou Institute of Advanced Studies, Zhejiang Normal University, Hangzhou 311231, China² Institute of Information Optics, Zhejiang Normal University, Jinhua 321004, China³ School of Engineering, Westlake University, Hangzhou 310024, China

* Correspondence: luosi@zjnu.edu.cn

† These authors contributed equally to this work.

Abstract: Highly sensitive and integrated optical multi-band CO₂ sensors are significant at the shortwave infrared (SWIR) region and still lack research. A compact CO₂ sensor composed of a Au-disk/TiO₂-cylinder/Au-film metasurface coated by polyhexamethylene biguanide (PHMB) film, functioning at multi-band resonances as well as having high sensitivity to gas concentrations, is presented. It can be employed as a dual-band narrowband absorber, producing two strongly resonant modes at the SWIR region under a reflection-type framework of linearly polarized incidence. Moreover, the metasurface sensor possesses high refractive index sensitivity of 109.25 pm/ppm at around 1040 nm and 42.57 pm/ppm at around 1330 nm in the range of 200–600 ppm, which is suitable for detecting atmospheric CO₂. Furthermore, the numerical results show that the sensitivity increases with a thicker PHMB film and optimizes at a thickness above 600 nm. The physical mechanism reveals that the higher order mode exhibits more extended near-field energy than the lower order mode, resulting in more sensitivity towards the surroundings. The design and results of our investigation show high-quality CO₂ sensing performance which functions at dual spectrum bands in the SWIR region and is promising for integrated photonic applications.



Citation: Long, W.; Zhou, R.; Du, Z.; Ling, Q.; Zhang, Y.; Zhao, D.; Shao, J.; Luo, S.; Chen, D. A Dual-Band Carbon Dioxide Sensor Based on Metal–TiO₂–Metal Metasurface Covered by Functional Material. *Photonics* **2022**, *9*, 855. <https://doi.org/10.3390/photonics9110855>

Received: 9 October 2022

Accepted: 1 November 2022

Published: 11 November 2022

Publisher's Note: MDPI stays neutral with regard to jurisdictional claims in published maps and institutional affiliations.



Copyright: © 2022 by the authors. Licensee MDPI, Basel, Switzerland. This article is an open access article distributed under the terms and conditions of the Creative Commons Attribution (CC BY) license (<https://creativecommons.org/licenses/by/4.0/>).

Keywords: metasurface; metal–insulator–metal; PHMB; carbon dioxide

1. Introduction

Gas detection has received widespread attention in environmental protection and climate change with the rapid pace of global urbanization and industrialization [1]. Carbon dioxide (CO₂), as one of fundamental greenhouse gases and essential components in industrial process, has been a critical concern over the last few decades [2]. Much effort has been carried out to realize specific CO₂ detection, and two major approaches, electrochemical methods [3] and nondispersive infrared (NDIR) technique [4], have been extensively adopted. Although electrochemical sensors are economical in the market and suitable for downsizing in portable applications, poor selectivity, hysteresis and harsh reaction conditions make them insufficient in highly sensitive, real-time, or special situations. Current NDIR gas sensors promise fast responses, but the centimeter- or millimeter-long optical interaction path to achieve high signal-to-noise ratio limits device integration, and the selectivity is still inadequate for complex gas detection in different spectral regions [5]. In particular, CO₂ absorption bands in the shortwave infrared (SWIR) spectral range from approximately 0.9 μm to 2.5 μm are sensitive down to the lowermost layers of the atmosphere, which tend to be affected by fluxes emitted from point sources [6,7]. Thus, SWIR gas sensors are essential in atmospheric monitoring, such as extensively used satellite and airborne hyperspectral imaging detection, which is indispensable to the estimation of natural phenomena and human activities.

Metasurfaces are a kind of artificial electromagnetic material with subwavelength scale character, which occupy numerous electromagnetic effects and are regarded as promising frequency-selective platforms for highly integrated, functionalized, and CMOS-compatible optical sensors [8,9]. Although metasurface emitters with high-quality-factor are achieved, the NDIR application scenario limits the miniaturization possibility of CO₂ sensors, and enhanced absorption characteristics with high selectivity have not been reported [10]. Several plasmonic metasurfaces covered by gas-sensitive polymer materials, such as polyethyleneimine, have demonstrated prominent electromagnetic resonances and selectively sensing features in the mid-infrared/visible spectrum region by interacting with the physically captured CO₂ molecules from their surroundings [11–13]. However, the sensing performance of this material is susceptible to environmental humidity, resulting in additional preprocessing procedures to deal with this polymer. For the SWIR probe, similar gas-selective-trapping polymer layers have been employed in fiber Bragg grating sensing installations to realize high chemical stability utilizing volume dilation of polyether sulfone in CO₂ exposure [14]. Nevertheless, the same humidity vulnerability exists, and the sensor is inadaptable for low concentration CO₂ detection in atmospheric environments.

Compared with other functional polymer materials, polyhexamethylene biguanide (PHMB) is advantageous to refractive index sensing, which is insensitive to humidity variation and can reversibly bind to CO₂ gas molecules via a simple alkali–acid interaction [15]. Theoretical work has been conducted to verify the sensing performance of this material covering grating slot waveguides [16]. In addition, experimental results exploiting microbubbles at fiber end have validated high CO₂ response selectivity of this material by sensing different types of gases (e.g., nitrogen, hydrogen, and argon) [17]. Unfortunately, these optical waveguide sensors under transmission type are not conducive to integration along the light path direction, and more importantly, the sensitivities are all below several tens of pm/ppm. A silicon disk metasurface based on reflection-type CO₂ detection downsizes the optical distance, whereas low sensitivity with only a single band of fundamental electromagnetic resonance is reported in the SWIR regime, which is not conducive to multi-frequency selected detection and is vulnerable to environmental disturbances without sufficient system stability [18,19]. Apart from these structures, metal–insulator–metal (MIM) metasurfaces are alternative platforms for supporting multiple resonant frequencies and combining functional gas-sensitive material [20]. The CMOS compatibility make them less difficult for mass production in contrast to nanostructures with 2D material, which generally need dedicated chemical vapor deposition growth and extra transfer procedures [21]. Therefore, highly sensitive and integrated optical sensors based on metasurface devices for multi-band CO₂ detection at the SWIR region are significant, but still lack research.

In this work, a compact CO₂ sensor composed of a metal–insulator–metal metasurface absorber coated with PHMB film with high sensitivity to gas concentration at dual resonant bands in the SWIR range is proposed. The insulator layer of this MIM structure is chosen to be TiO₂, which has a high refractive index at the visible/SWIR region compared to the common metal oxide interlayers such as Al₂O₃ or SiO₂ [22]. The metasurface is formed by a Au-disk/TiO₂-cylinder/Au-film array on a silica substrate. This configuration offers the possibility to be employed as a dual-band narrowband absorber, producing two strongly resonant modes at around 858.56 nm and 1254.35 nm in the near-infrared band. Moreover, the metasurface possesses high refractive index sensitivity, indicating 109.25 pm/ppm at ~1040 nm and 42.57 pm/ppm at ~1330 nm when coated with the functional host material PHMB for CO₂ concentration detection. Furthermore, the numerical results show that the sensitivity increases with a thicker PHMB film and optimizes with a PHMB thickness above 600 nm. The design and results of our investigation show high-quality CO₂ sensing performance which functions at dual channel in the SWIR region and occupies competitive sensitivity, which is promising for integrated photonic and CMOS-compatible gas-sensing applications.

2. Design and Simulation Method

Metasurfaces can be described by complex electric permittivity and magnetic permeability. By regulating the effective impedance determined by metasurface design parameters, it is conceivable to obtain specific electromagnetic characteristics exhibiting tremendous merits over conventional predecessors due to its compact size and extraordinary features. Our design is inspired by the MIM resonators supporting diversified waveguide modes when the transverse dimension along the polarization direction changes [23,24]. Such modes are tightly concentrated so that the evanescent tail is short and strongly overlaps with the subwavelength scale molecules which are bounded around the structural localized volume.

Figure 1 shows a schematic diagram of the proposed metasurface carbon dioxide gas sensor with periodical Au-disk/TiO₂-cylinder/Au-film cells, which define the three layers of the resonator. Instead of a continuous insulator film to restrict the near fields inside the interlayer of the resonator [23], a discrete insulator layer (TiO₂-cylinder) is employed to expand the interaction area between the evanescent fields and the gas molecules to be detected. Accounting for the practical application, the unit cell was located on the top of the SiO₂ substrate with a refractive index of 1.45. The thicknesses of the Au disks and TiO₂ nanocylinders are represented by H₁ and H₂, and their radius is r. The thickness of the Au layer is represented with D. P_x and P_y represent the period length of a unit cell in the x- and y- directions, respectively. The geometric parameters are fixed at P_x = P_y = 650 nm, r = 270 nm, H₁ = 25 nm, H₂ = 40 nm.

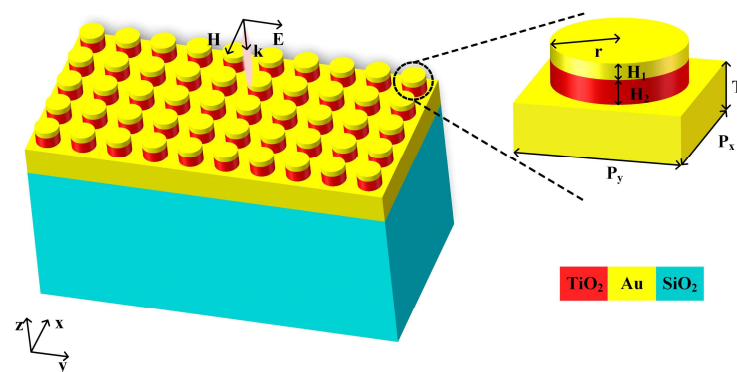


Figure 1. Schematic of the proposed metasurface and the enlarged view of the unit-cell.

A plane wave polarized in the y direction at normal incidence is exploited to investigate the optical properties of the symmetric structure under random linear polarized incidence as shown in Figure 1. The Au film is modeled as a perfect electric conductor (PEC) to prevent the electromagnetic wave from penetrating in the near-infrared range, and the transmission is nearly null. The optical spectrum and the electromagnetic field features are calculated by three-dimensional (3D) full-wave simulations utilizing the finite element method (FEM). In the FEM simulations, the effect of weak transmission and calculated absorbance (A) is considered using both reflectance (R) and transmittance (T) from the following relationship: $A = 1 - R - T$. To reduce computational memory, we calculate a single unit-cell by setting a periodic boundary condition on the lateral sides of the design. The proposed metasurface configuration is positioned between the source port and the output port. Perfectly matched layers (PMLs) are applied in the inner boundaries to diminish the electromagnetic wave propagating in the direction perpendicular to the port boundary. The electric permittivity and magnetic permeability parameters of Au and TiO₂ are referenced from [25,26].

3. Results and Discussion

3.1. Absorption Properties and Resonance Characterization

The transmission, reflection and absorption spectra of the proposed metamaterial have been calculated from 800 nm to 1400 nm in the near-infrared region shown as Figure 2. Two resonances, mode 1 and mode 2, with the central wavelengths $\lambda_1 = 1254.35$ nm and $\lambda_2 = 858.56$ nm are excited. The max absorption intensities are $I_1 = 88.1\%$ and $I_2 = 84.5\%$ when the surrounding medium is air. The transmission is nearly zero, which means the absorption spectra of the proposed metasurface can be obtained by simply measuring the light reflection in the experiments. From the FEM model, it is noted that the reflection dip intensity and the spectral peak position depend on the period and the thickness of the top metal and the insulator layer. Although the intrinsic dual-mode absorption spectra of the metasurface are not the strongest, the structure parameters are chosen to obtain intense resonances at the SWIR region when coated with CO₂-sensitive layer, which is discussed in the sensing performance section.

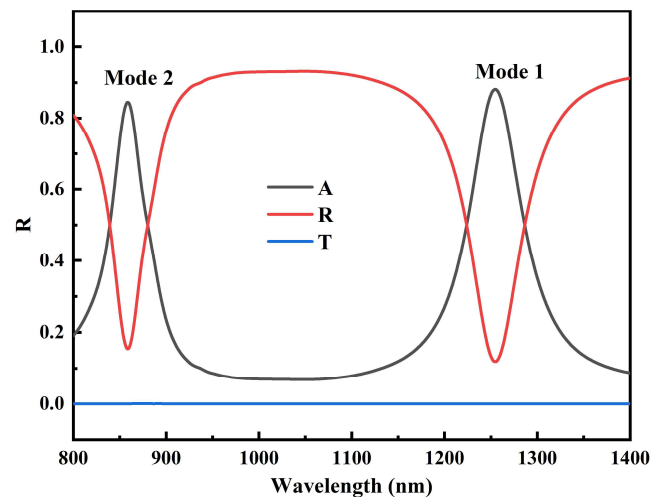


Figure 2. Absorption (A), reflection (R) and transmission (T) spectra of the proposed metasurface.

To explain the physical mechanism more clearly for the two absorption peaks, the electric ($|E|$) and magnetic ($|H|$) field distributions of mode 1 and mode 2 in different planes are calculated as shown in Figure 3. The operation of the MIM resonator can be understood using a Fabry–Perot model [24], in which the slow gap plasmons excited along the polarized y-direction are reflected at either end of the top metal feature. Different from the fundamental plasmonic mode in MIM metasurface with only a single “hot spot” in the magnetic field distribution [24,27], the two modes demonstrate two symmetric higher-order waveguide modes in the SWIR band.

Within the Fabry–Perot picture, the longer wavelength resonance (mode 1) is described as a standing wave pattern along the y-direction created by the bouncing between the nanoparticle facets at $y = -R$ and $y = R$, whose electric (Figure 3a,b) and magnetic (Figure 3e,f) field distribution cross-sections are represented. The white arrows in Figure 3a,e manifest the corresponding directions of $|E|$ and $|H|$ field distributions in the x-y plane at the insulator interior, indicating that the electric charge oscillation of the excited localized surface plasmon resonance (LSPR) are restricted by the incident polarization and the circular outline of the structure. It is noteworthy that most near-field energy is confined in the intermediate dielectric TiO₂ layer, as depicted in Figure 3b,f.

Compared with mode 1, mode 2, shown in the lower row of Figure 3, is considered to be a higher-order mode of LSPR between the topmost Au disk and the reflector layer, owing to the shorter wavelength resonance and denser electric charge distributions. According to the data in Figure 3d,h, more light energy in mode 2 penetrates into the ambient medium and couples with adjacent nano-disks revealed by the brighter color map distributed in the

top Au and the surroundings when compared to Figure 3b,f of mode 1, respectively. That means the higher-order mode (mode 2) is a comparatively extended SPR mode, whereas the lower-order mode (mode 1) is a more confined mode, which exhibits relatively higher absorption ($I_1 > I_2$) by the structure in the SWIR spectra region. In this paper, the sensing performance resulting from the different resonance/absorption mechanisms of two intrinsic resonant modes in the proposed metasurface absorber is discussed.

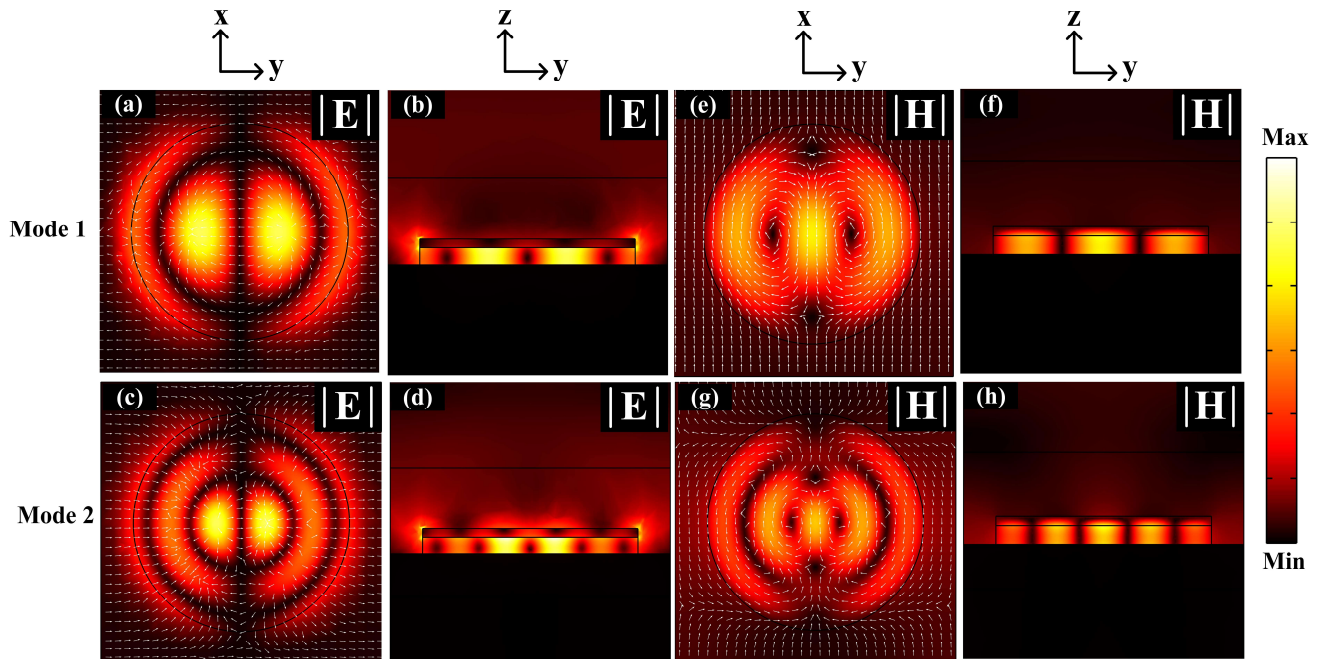


Figure 3. The normalized electric and magnetic field profiles corresponding to the two resonant modes. (a–d) represent the electric field ($|E|$) distributions of mode 1 in x-y (a), y-z (b) plane and mode 2 in x-y (c), y-z (d) plane. (e–h) represent the magnetic field ($|H|$) distributions of mode 1 in x-y (e), y-z (f) plane and mode 2 in x-y (g), y-z (h) plane. The white arrows manifest the corresponding directions of $|E|$ (a,c) and $|H|$ (e,g) field distributions in x-y plane at the insulator center.

3.2. Sensing Performance

The influence of the surrounding medium refractive index (RI) on the absorption properties of the proposed metasurface and its sensing performance is further investigated. To explore the possibility of gas sensing using the proposed metasurface, the refractive index change range surrounding the metasurface is set from 1.48 to 1.54 considering the RI variation of PHMB polymer when sensing CO_2 gas concentration in this simulation [28]. The sensitivity is linearly fitted to 2.024×10^{-4} RIU/ppm in the detection range of 200–600 ppm according to this previous study.

Figure 4a presents the central reflection wavelength of the two resonant modes when the ambient refractive index changes considering $R = 1 - A$ and reflection is feasible to be detected in practice. Mode 1 demonstrates that the reflection/absorption peaks possess red-shift from 1324.93 nm to 1337.55 nm as pointed out in Figure 4b, and mode 2 shows that the reflection/absorption peaks possess red-shift from 1027.54 nm to 1060.01 nm. The absorption intensity of mode 1 reaches up to 0.988, close to a perfect absorber and nearly remains constant when the RI of PHMB varies. The absorption intensity of mode 2 reaches 0.925 when the refractive index of PHMB is 1.48, and indicates a slight decrease with larger RI of PHMB. The variations in resonant wavelength are linearly fitted as a function of medium refractive index in Figure 4a, demonstrating high refractive index sensitivity of 541.16 nm/RIU for mode 1 and 210.35 nm/RIU for mode 2. The CO_2 concentration

sensitivity of the proposed structure combined with PHMB gas-sensitive materials can be expressed as:

$$S(\text{pm/ppm}) = \frac{\Delta\lambda}{\Delta c} \tag{1}$$

where $\Delta\lambda$ is the center wavelength change in resonance modes and Δc is the corresponding CO₂ gas concentration change which results in PHMB refractive index change impacting the resonances. According to Equation (1), the sensitivity of CO₂ gas sensing for mode 1 and mode 2 is calculated to be $S_1 = 42.57$ pm/ppm and $S_2 = 109.25$ pm/ppm, respectively.

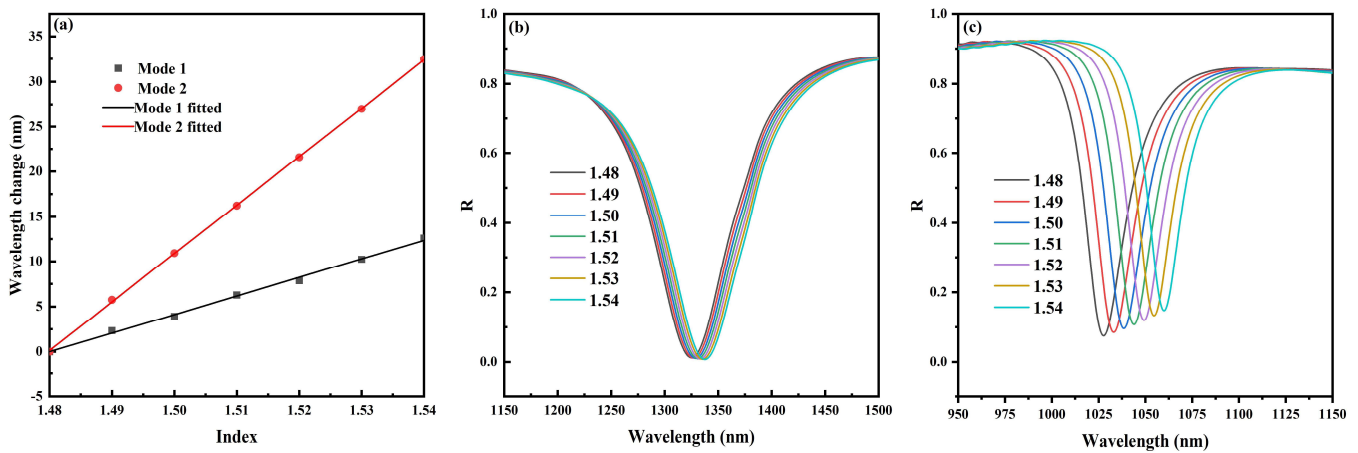


Figure 4. (a) The absorption peak wavelength of mode 1 (b) and mode 2 (c) with surrounding RI changing from 1.48 to 1.54.

Therefore, when exposed in a gas-sensitive medium of high RI, the proposed metasurface absorber demonstrates superior spectra performance (absorptivity) in the SWIR range, with the higher-order mode (mode 2, extended LSPR mode) being more sensitive towards the surroundings than the lower-order mode (mode 1, confined mode). Furthermore, to highlight the excellent performance of the proposed structure, a detailed comparison with other optical RI-based CO₂ gas sensors is summarized in Table 1. It is worth noting that the two resonant modes, which can be simultaneously used for CO₂ gas sensing, are not revealed in other reports. In addition, the features of high sensitivity in the SWIR region under compact reflection-type with humidity insensitive gas gathering layer make the proposed sensing system conspicuous.

Table 1. Comparison of CO₂ sensing performance between this and previous work based on gas-sensitive polymer materials.

Structure	Gas Trapping Layer	Sensitivity (pm/ppm)	Resonant Spectrum Region (nm)		Operation Type	Humidity Insensitive	Ref.
Graphene-ribbon metasurface	Polyethylenimine	\	6300–6800	Mid-infrared	Transmission	No	[12]
Au-Al ₂ O ₃ -Au metasurface	Polyethylenimine	3–8	600–700	Visible	Reflection	No	[13]
Fiber Bragg grating	Polyether sulfone	0.77×10^{-4}	\	\	Transmission	No	[14]
Silicon microring	PHMB	3.5×10^{-3}	1552.5–1552.6	SWIR	Transmission	Yes	[15]
Grating slot	PHMB	12.9	1540–1600	SWIR	Transmission	Yes	[16]
Fiber microbubble	PHMB	0.46	1531.7–1531.9	SWIR	Transmission	Yes	[17]
Si-disk metasurface	PHMB	17.3	910–990	SWIR	Reflection	Yes	[18]
Fiber Fabry–Perot cavity	PHMB	12.2	1560–1570	SWIR	Reflection	Yes	[29]

Table 1. Cont.

Structure	Gas Trapping Layer	Sensitivity (pm/ppm)	Resonant Spectrum Region (nm)		Operation Type	Humidity Insensitive	Ref.
Microtube	Zeolitic imidazolate framework-8	7.4×10^{-4}	630–670	Visible	Reflection	Yes	[30]
Au-TiO ₂ -Au metasurface	PHMB	42.57	1324.93–1337.55	SWIR	Reflection	Yes	This paper
		109.25	1027.54–1060.01				

Finally, to improve application feasibility, the effect of PHMB gas-sensitive materials thickness (D) on CO₂ gas sensing is calculated as shown in Figure 5. It indicates that the sensing sensitivity increases as D increases, but the increase rate of sensitivity slows down as the thickness increases. When D is greater than 600 nm, increasing D for sensitivity rise does not help significantly. Moreover, when D = 900 nm, the sensitivity of CO₂ gas sensing is close to the situation that the metasurface is completely immersed in the PHMB environment discussed in Figure 4 above.

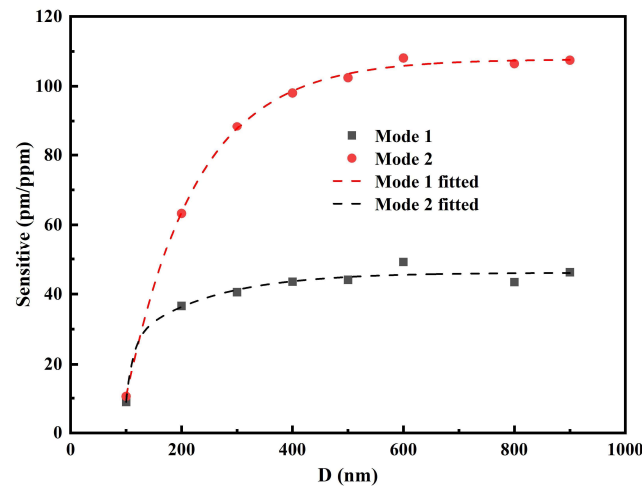


Figure 5. CO₂ concentration sensitivity varies as a function of PHMB thickness (D). To unveil the behind physics, the electric field distributions of mode 1 and mode 2 in different planes when PHMB thickness is 200 nm and 900 nm are shown in Figure 6. When the metasurface is covered by a PHMB layer, the light energy of the extended mode (mode 2, Figure 6h,i,k,l) spreads to the high refractive index gas-trapping layer, resulting in sufficient interaction with the surroundings. Nevertheless, most near fields of the confined mode (mode 1, Figure 6b,c,e,f) are still concentrated tightly inside the resonator. Accordingly, the RI sensitivity of mode 2 is much higher than mode 1.

When the thickness of PHMB is thin (e.g., D = 200 nm), the near-field energy also permeates into the ambient air above PHMB (Figure 6b,c,h,i). When D is increased (e.g., D = 900 nm), more energy is gathered inside the PHMB layer issuing in increased RI sensitivity, which is evident by Figure 6k,l,e,f. Moreover, the increased effect of PHMB thickness on sensitivity is more pronounced in mode 2 than mode 1 as shown in Figure 5, because of the more dispersive field distributions of mode 2 revealed by the contrast of Figure 6k,e. In practice, the thickness of PHMB influences the response time to gather CO₂ gas for adequate reaction [28,29]. Therefore, the optimum thickness of PHMB gas-sensitive materials needs to be determined in experiments by measuring the relationship between PHMB thickness and response time.

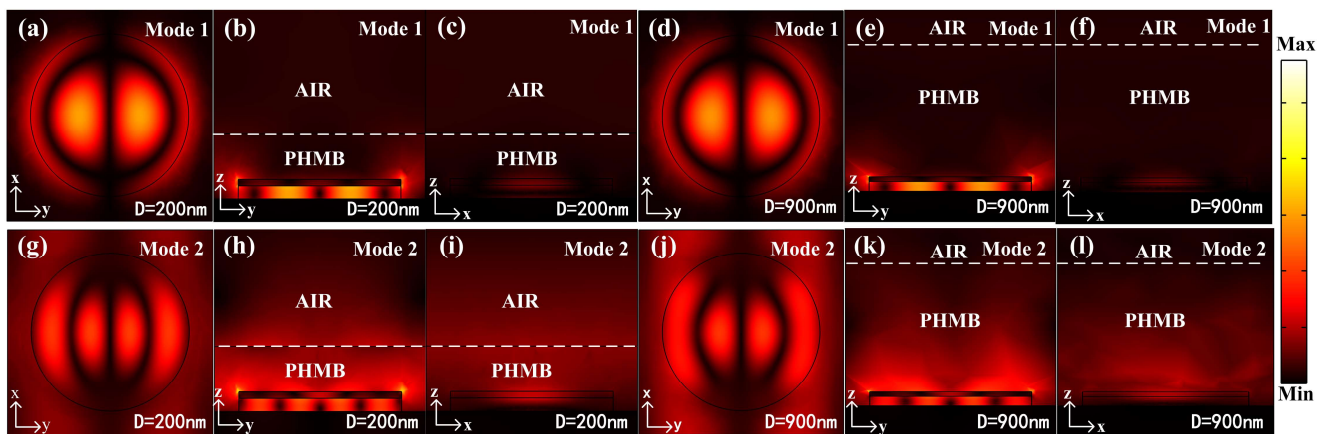


Figure 6. The normalized electric field profiles corresponding to the two resonant modes when the PMHB thickness is 200 nm and 900 nm. (a–f) represent the electric field distributions of mode 1 for $D = 200$ nm in x–y (a), y–z (b) and z–x (c) plane, and $D = 900$ nm in x–y (d), y–z (e) and z–x (f) plane. (g–l) represent the electric field distributions of mode 2 for $D = 200$ nm in x–y (g), y–z (h) and z–x (i) plane, and $D = 900$ nm in x–y (j), y–z (k) and z–x (l) plane. The white dashed lines show the interface of PHMB layer and air. The figures in y–z plane have been scaled to display the complete thickness.

4. Discussion

The numerically simulated results of this proposed sensor rely on the previously measured data of the functional PHMB material with experiments conducted in the SWIR region. Therefore, sensing performances presented here focus on the similar spectra band as well as the same detection range of 200–600 ppm which is critical and suitable for atmospheric CO₂ detection. More experiment data of PHMB features relating to CO₂ concentration is essential for different working band and larger detection range. In addition, the sensing performance also depends on the exact MIM metasurface parameters, which are affected by the fabrication quality and accuracy. It is worth highlighting that this classical MIM structure can be feasibly realized by nanofabrication methods [31]. After deposition of the lower layer gold film onto the substrate, photoresist can be spin-coated and exposed to an electron-beam to be nanopatterned. After development, the interlayer TiO₂ and the top Au film can be deposited onto the patterned photoresist. Following that, the MIM metasurface can be obtained after lift-off to remove the resist layer. Finally, the proposed sensor can be realized by spin-coating PHMB onto this metasurface.

5. Conclusions

In summary, this paper has presented a compact CO₂ sensor composed of a metal–insulator–metal metasurface coated by PHMB film functioning at multi-band resonances as well as having high sensitivity to gas concentration. The metasurface is formed by a Au-disk/TiO₂-cylinder/Au-film array on a silica substrate. It can be employed as a dual-band narrowband absorber, producing two strongly resonant modes at the SWIR region under a reflection-type framework of linearly polarized incidence. Moreover, the metasurface sensor possesses high refractive index sensitivity of 109.25 pm/ppm at around 1040 nm and 42.57 pm/ppm at 1330 nm. Furthermore, the numerical results show that the sensitivity increases with a thicker PHMB film and optimizes with a PHMB thickness above 600 nm. The physical mechanism of sensing performance differences between the lower order mode (the confined mode 1) and the higher order mode (the extended mode 2) have been discussed in detail. The design and results of our investigation show competitive dual-band CO₂ sensing performance, providing significant guidance for SWIR integrated photonic sensing applications.

Author Contributions: Conceptualization, W.L. and S.L.; data curation, W.L., R.Z. and Z.D.; formal analysis, S.L. and Q.L.; funding acquisition, S.L.; methodology, R.Z. and Z.D.; project administration, J.S.; resources, Q.L. and J.S.; supervision, S.L. and D.C.; visualization, R.Z. and Y.Z.; writing—original draft, W.L.; writing—review and editing, R.Z., S.L., Y.Z., D.Z. and D.C. All authors have read and agreed to the published version of the manuscript.

Funding: This research was funded by the Zhejiang Provincial Natural Science Foundation of China (Grant No. LQ22F050007); the “Pioneer” and “Leading Goose” R&D Program of Zhejiang (Grant No. 2022C03084 and 2022C03066).

Institutional Review Board Statement: Not applicable.

Informed Consent Statement: Not applicable.

Data Availability Statement: Not applicable.

Conflicts of Interest: The authors declare no conflict of interest.

References

1. Zhao, P.; Zhao, Y.; Bao, H.; Ho, H.L.; Jin, W.; Fan, S.; Gao, S.; Wang, Y.; Wang, P. Mode-phase-difference photothermal spectroscopy for gas detection with an anti-resonant hollow-core optical fiber. *Nat. Commun.* **2020**, *11*, 847. [[CrossRef](#)]
2. Pang, J.; Le, X.; Pang, K.; Dong, H.; Zhang, Q.; Xu, Z.; Gao, C.; Fu, Y.; Xie, J. Highly precision carbon dioxide acoustic wave sensor with minimized humidity interference. *Sens. Actuators B Chem.* **2021**, *338*, 129824. [[CrossRef](#)]
3. Srinives, S.; Sarkar, T.; Hernandez, R.; Mulchandani, A. A miniature chemiresistor sensor for carbon dioxide. *Anal. Chim. Acta* **2015**, *874*, 54–58. [[CrossRef](#)] [[PubMed](#)]
4. Dinh, T.-V.; Choi, I.-Y.; Son, Y.-S.; Kim, J.-C. A review on non-dispersive infrared gas sensors: Improvement of sensor detection limit and interference correction. *Sens. Actuators B Chem.* **2016**, *231*, 529–538. [[CrossRef](#)]
5. Pusch, A.; De Luca, A.; Oh, S.S.; Wuestner, S.; Roschuk, T.; Chen, Y.; Boual, S.; Ali, Z.; Phillips, C.C.; Hong, M.; et al. A highly efficient CMOS nanoplasmonic crystal enhanced slow-wave thermal emitter improves infrared gas-sensing devices. *Sci. Rep.* **2015**, *5*, 17451. [[CrossRef](#)] [[PubMed](#)]
6. Romaniello, V.; Spinetti, C.; Silvestri, M.; Buongiorno, M.F. A Methodology for CO₂ Retrieval Applied to Hyperspectral PRISMA Data. *Remote Sens.* **2021**, *13*, 4502. [[CrossRef](#)]
7. Xia, X.; Zou, X. Development of CO₂ Band-Based Cloud Emission and Scattering Indices and Their Applications to FY-3D Hyperspectral Infrared Atmospheric Sounder. *Remote Sens.* **2020**, *12*, 4171. [[CrossRef](#)]
8. Wang, Y.; Landreman, P.; Schoen, D.; Okabe, K.; Marshall, A.; Celano, U.; Wong, H.-S.P.; Park, J.; Brongersma, M.L. Electrical tuning of phase-change antennas and metasurfaces. *Nat. Nanotechnol.* **2021**, *16*, 667–672. [[CrossRef](#)]
9. Zhang, Y.; Liu, H.; Cheng, H.; Tian, J.; Chen, S. Multidimensional manipulation of wave fields based on artificial microstructures. *Opto-Electron. Adv.* **2020**, *3*, 200002. [[CrossRef](#)]
10. Miyazaki, H.T.; Kasaya, T.; Iwanaga, M.; Choi, B.; Sugimoto, Y.; Sakoda, K. Dual-band infrared metasurface thermal emitter for CO₂ sensing. *Appl. Phys. Lett.* **2014**, *105*, 121107. [[CrossRef](#)]
11. Hasan, D.; Lee, C. Hybrid Metamaterial Absorber Platform for Sensing of CO₂ Gas at Mid-IR. *Adv. Sci.* **2018**, *5*, 1700581. [[CrossRef](#)]
12. Bareza, N.J.; Gopalan, K.K.; Alani, R.; Paulillo, B.; Pruneri, V. Mid-infrared Gas Sensing Using Graphene Plasmons Tuned by Reversible Chemical Doping. *ACS Photon.* **2020**, *7*, 879–884. [[CrossRef](#)]
13. Pohl, T.; Sterl, F.; Strohhfeldt, N.; Giessen, H. Optical Carbon Dioxide Detection in the Visible Down to the Single Digit ppm Range Using Plasmonic Perfect Absorbers. *ACS Sens.* **2020**, *5*, 2628–2635. [[CrossRef](#)]
14. Zhou, Z.; Xu, Y.; Qiao, C.; Liu, L.; Jia, Y. A novel low-cost gas sensor for CO₂ detection using polymer-coated fiber Bragg grating. *Sens. Actuators B Chem.* **2021**, *332*, 129482. [[CrossRef](#)]
15. Mi, G.; Horvath, C.; Aktary, M.; Van, V. Silicon microring refractometric sensor for atmospheric CO₂ gas monitoring. *Opt. Express* **2016**, *24*, 1773–1780. [[CrossRef](#)]
16. Badri, S.H. Transmission resonances in silicon subwavelength grating slot waveguide with functional host material for sensing applications. *Opt. Laser Technol.* **2020**, *136*, 106776. [[CrossRef](#)]
17. Li, H.; Sun, B.; Yuan, Y.; Yang, J. Guanidine derivative polymer coated microbubble resonator for high sensitivity detection of CO₂ gas concentration. *Opt. Express* **2019**, *27*, 1991–2000. [[CrossRef](#)]
18. Kazanskiy, N.L.; Butt, M.A.; Khonina, S.N. Carbon Dioxide Gas Sensor Based on Polyhexamethylene Biguanide Polymer Deposited on Silicon Nano-Cylinders Metasurface. *Sensors* **2021**, *21*, 378. [[CrossRef](#)]
19. Yu, S.; Zhang, Z.; Li, M.; Xia, H. Multi-frequency differential absorption lidar incorporating a comb-referenced scanning laser for gas spectrum analysis. *Opt. Express* **2021**, *29*, 12984–12995. [[CrossRef](#)]
20. Chen, K.; Adato, R.; Altug, H. Dual-Band Perfect Absorber for Multispectral Plasmon-Enhanced Infrared Spectroscopy. *ACS Nano* **2012**, *6*, 7998–8006. [[CrossRef](#)]

21. Zeng, C.; Lu, H.; Mao, D.; Du, Y.; Hua, H.; Zhao, W.; Zhao, J. Graphene-empowered dynamic metasurfaces and metadevices. *Opto-Electron. Adv.* **2022**, *5*, 200098. [[CrossRef](#)]
22. Wu, Y.; Yang, W.; Fan, Y.; Song, Q.; Xiao, S. TiO₂ metasurfaces: From visible planar photonics to photochemistry. *Sci. Adv.* **2019**, *5*, eaax0939. [[CrossRef](#)] [[PubMed](#)]
23. Duffett, G.; Wirth, R.; Rayer, M.; Martins, E.; Krauss, T.F. Metal-insulator-metal nanoresonators—Strongly confined modes for high surface sensitivity. *Nanophotonics* **2020**, *9*, 1547–1552. [[CrossRef](#)]
24. Yang, J.; Sauvan, C.; Jouanin, A.; Collin, S.; Pelouard, J.-L.; Lalanne, P. Ultrasmall metal-insulator-metal nanoresonators: Impact of slow-wave effects on the quality factor. *Opt. Express* **2012**, *20*, 16880–16891. [[CrossRef](#)]
25. Abbas, M.A.; Zubair, A.; Riaz, K.; Huang, W.; Teng, J.; Mehmood, M.Q.; Zubair, M. Engineering multimodal dielectric resonance of TiO₂ based nanostructures for high-performance refractive index sensing applications. *Opt. Express* **2020**, *28*, 23509–23522. [[CrossRef](#)]
26. Johnson, P.B.; Christy, R.W. Optical Constants of the Noble Metals. *Phys. Rev. B* **1972**, *6*, 4370. [[CrossRef](#)]
27. Carrara, A.; Maccaferri, N.; Cerea, A.; Bozzola, A.; De Angelis, F.; Proietti Zaccaria, R.; Toma, A. Plasmon hybridization in compressible metal-insulator-metal nanocavities: An optical approach for sensing deep sub-wavelength deformation. *Adv. Opt. Mater.* **2020**, *8*, 2000609. [[CrossRef](#)]
28. Koushik, K.P.; Malathi, S. Optical micro-ring resonator for detection of carbon dioxide gas. In *Emerging Trends in Photonics, Signal Processing and Communication Engineering*; Springer Nature Singapore Pte Ltd.: Singapore, 2020; pp. 157–161.
29. Ma, W.; Xing, J.; Wang, R.; Rong, Q.; Zhang, W.; Li, Y.; Zhang, J.; Qiao, X. Optical Fiber Fabry–Perot Interferometric CO₂ Gas Sensor Using Guanidine Derivative Polymer Functionalized Layer. *IEEE Sens. J.* **2018**, *18*, 1924–1929. [[CrossRef](#)]
30. Kong, Y.; Zhao, Z.; Wang, Y.; Yang, S.; Huang, G.; Wang, Y.; Liu, C.; You, C.; Tan, J.; Wang, C.; et al. Integration of a Metal–Organic Framework Film with a Tubular Whispering-Gallery-Mode Microcavity for Effective CO₂ Sensing. *ACS Appl. Mater. Interfaces* **2021**, *13*, 58104–58113. [[CrossRef](#)]
31. Yamada, H.; Kawasaki, D.; Sueyoshi, K.; Hisamoto, H.; Endo, T. Fabrication of Metal-Insulator-Metal Nanostructures Composed of Au-MgF₂-Au and Its Potential in Responding to Two Different Factors in Sample Solutions Using Individual Plasmon Modes. *Micromachines* **2022**, *13*, 257. [[CrossRef](#)]